Delft University of Technology

Modeling the interaction of carbon segregation to defects and carbon partitioning in multiphase steels

Traka, Konstantina; Sietsma, Jilt; Santofimia Navarro, Maria J.

Important note
To cite this publication, please use the final published version (if applicable).
Please check the document version above.

Full length article

Modeling the interaction of carbon segregation to defects and carbon partitioning in multiphase steels

Konstantina Traka *, Jilt Sietsma, Maria J. Santofimia Navarro

Department of Materials Science and Engineering, TU Delft, Mekelweg 2, 2628 CD Delft, The Netherlands

ARTICLE INFO

ABSTRACT

Carbon segregation to defects in martensite is a phenomenon known for its occurrence and interference with mechanisms such as carbon partitioning in multiphase steels. Especially in martensite–austenite partitioning processes, carbon trapping at/de-trapping from martensite defects plays an important role since it interacts with the austenite enrichment. In this work, we develop a physics-based model in which we incorporate the concurrent evolution of carbon partitioning and trapping at/de-trapping from martensite defects. The model describes the global and local, time-dependent distribution of carbon between three lattice types, namely martensite defects, martensite solid solution, and austenite. We implement the model in mean-field and full-field descriptions, and discuss the interaction between carbon enrichment in austenite and segregation to martensite defects, on the basis of global equilibrium as well as on the carbon kinetics. We apply the model in several martensite — austenite microstructures and discuss the dependence of the interaction between carbon partitioning and trapping at/de-trapping from defects on specific microstructural features, i. e. phase fractions and microstructural banding.

1. Introduction

Solute segregation to dislocations and grain boundaries is a well known phenomenon regarding its impact, whether this is desired or undesired, on the material performance, e. g. mechanical [1], electrical [2], corrosion properties [3]. Despite its direct consequences for the material properties, solute segregation to defects interferes with specific physical processes [4] and hence microstructural evolution and treatment goals, thereby affecting once again the material properties. Specifically in martensite-based iron alloys, carbon trapping at defects is an integral part of almost any treatment and microstructure, including quenching [5], aging [6], austenite reversion, stabilization or partitioning treatments [7,8], and tempering [9].

When it comes to carbon partitioning in austenite–martensite microstructures, the current physics-based modeling approaches, e. g. [10–12], typically ignore the effect of carbon trapping at martensite defects. Instead, martensite is treated as a strain-free body-centered cubic (BCC) phase, i. e. identical to ferrite, regarding the chemical potential of carbon. This means that the solubility of carbon in martensite is underestimated and the austenite enrichment overestimated. In more recent works [13,14], the carbon trapping at martensite defects during partitioning was incorporated, but the carbon concentration in martensite defects was kept unchanged during the simulated partitioning. However, the amount of carbon trapped at defects is proportional to the

amount of carbon in solid solution [15–20], meaning that if the carbon concentration in the solid solution of martensite changes due to partitioning, the trapped-carbon concentration should change accordingly, and vice versa. Essentially, the approaches of Dai et al. [13], Pohjonen et al. [14] corrected for the solubility of carbon in martensite as an individual phase, but neglected that the trapped carbon concentration should be adjusted from the changes in the free-carbon concentrations due to phase partitioning. In this view, the effect of carbon segregation to defects on partitioning is overestimated. Therefore, predicting the carbon enrichment of austenite requires also the concurrent evolution of carbon trapping at, and de-trapping from martensite defects. Moreover, there is much evidence [7,21] that already in the quenched state almost all carbon in martensite is trapped at dislocations and boundaries, whereas high carbon enrichment of austenite has been confirmed [22]. Hence, in practice, for carbon enrichment in austenite, carbon needs to de-trap from martensite defects during annealing. For this reason, we propose a physics-based model for the interaction between carbon partitioning and segregation to defects.

The theories describing carbon segregation to defects as a function of the carbon concentration in the adjacent undefected lattice are well-known. One way or another, i.e. the so-called Cottrell atmospheres or carbon-rich boundaries, encompass defected regions (e. g. strained

lattice regions or dislocations and grain boundaries) that host excess carbon atoms. This excess comes from the thermodynamic equilibrium of carbon between the defected region and the adjacent lattice. The equilibrium concentrations are typically addressed by considering the chemical potentials of the solute atoms within the dislocation strain field [23] and the adjacent unstrained lattice [16–18], or based on the interface/bulk balance of adsorption and desorption rates, i.e. following the Langmuir–McLean isotherm [24,25]. Either way, the extent of solute segregation, locally and hence overall as well, is proportionally related with the concentration of carbon in the solid solution of the abutting perfect lattice [15,19,20]. This means that any microstructural process entailing a redistribution of carbon in solid solution at mesoscale distances (e.g. diffusion due to partitioning) is expected to interact with carbon segregation to defects. The more carbon is trapped, the less carbon is in solid solution, and vice versa. Specifically for martensite–austenite microstructures, the solid solution redistribution between two phases of different solubility, is realized through interphase partitioning [26], which dictates the carbon concentration in martensite to decrease. Therefore, coupling the theoretical description of carbon equilibrium between lattice and defects, and between two phases of different solubility, already indicates that carbon trapping to martensite defects changes during (and interacts with) partitioning.

For this reason, in the present work we describe the mesoscale carbon redistribution under the consideration of carbon trapping at and de-trapping from defects as an interactive phenomenon, by coupling the fundamentals of each concurring process. Without loss of generality, here we apply the model in cases where the carbon redistribution is caused by interface partitioning and/or the trapped carbon itself that is heterogeneously distributed, e.g. lath boundaries vs. bulk martensite. We propose a coupled description of the evolution and interaction of carbon defect trapping and interphase partitioning. The model describes (a) the equilibrium state (i.e. mean field), and (b) the local and temporal evolution (i.e. numerical) of the associated processes. The latter is used to assess the time-dependent and topological interplay between the different phenomena. The input microstructures are obtained from electron backscatter diffraction (EBSD) and are characterized by different microstructural features, local and average, since these affect the carbon diffusion [27,28] as well as the equilibrium state. The model description is given in Section 2, including the application on an artificial microstructure such that the evolution of the carbon concentration-related variables in space and time, based on the present approach, becomes clear. Section 3 applies the model to experimental martensite–austenite microstructures determined by means of EBSD.

2. Model description

2.1. Theory

The current approach for carbon partitioning including segregation to defects, whether described numerically or analytically, is such that the chemical potential of carbon, μ_C, becomes equal everywhere, i.e. $\nabla \mu_C = 0$. The incorporation of carbon segregation to defects is realized by considering martensite as a phase different from ferrite, in the sense that martensite accommodates two different lattice types, i.e. unstrained sites (equivalent to ferrite) and defects (dislocations and boundaries).

The physical mechanisms that concur and thus are described in the model are:

- the carbon in solid solution obeying always the concentration-gradient driven (long-range) diffusion [29], realized at the mesoscale,
- the partitioning of carbon at the martensite–austenite interfaces to match the (local) phase equilibrium concentrations [26],
- the carbon partitioning between the lattice and defects such that it matches the proportionally related [16–18,24,25] concentrations of trapped and free carbon.

2.2. Independent and constitutive state variables

2.2.1. Model system

The two-dimensional[1] simulated microstructures consist of elementary volumes i, which have the following properties.

- A position vector in the two-dimensional xy grid: $\bar{z}_i$.
- A phase parameter p_i, taking values $p_i = 0$ for austenite (γ) and $p_i = 1$ for martensite (α').
- Its carbon concentration $x_{C,i}^{tot}$.
- Its defect concentration ρ_i. Grain boundaries and dislocations are both crystallographic defects that can trap carbon. We do not distinguish between these two types, but define a single defect density with the unit m^{-2}, in line with the dislocation density.

The initial microstructure considered as starting point for the simulations is a state after quenching a fully austenitic material, during which a certain fraction of the austenite transforms to martensite. The phase fractions are hereafter denoted as $f^{\alpha'}$ for martensite and f^γ for austenite. In the initial martensite–austenite microstructure the overall carbon concentration x_C^{tot} is homogeneous. The carbon concentration $x_{C,i}^{tot}$ of each martensitic element i within the modeled microstructure is partly trapped at defects, partly free as interstitial solid solution in the iron lattice. These two concentrations are denoted as $x_{C,i}^{free}$ and $x_{C,i}^{trap}$, respectively. The total carbon concentration of each material element i is:

$$x_{C,i}^{tot} = x_{C,i}^{free} + x_{C,i}^{trap}. \tag{1}$$

At any simulation step, trapped carbon cannot undergo diffusion through the lattice, free carbon can. However, trapped carbon is always in equilibrium with the free carbon at the same elementary unit i, and it thus changes accordingly, as will be explained later.

Carbon trapping at austenite defects is neglected for two reasons. First, because the solubility of carbon in austenite is much higher than in strain-free martensite (i.e. ferrite), meaning that there is less need for carbon in austenite to relax the lattice by accommodating at its defects, in comparison to the case of martensite. Therefore, the defect enrichment is much less in austenite compared to martensite. Secondly, the defect density of austenite is much lower compared to martensite.

2.2.2. Free- and trapped-carbon concentration

Each elementary unit i has a free-carbon concentration $x_{C,i}^{free}$, which evolution in time is determined by diffusion and partitioning, as will be discussed later in this section. In addition, martensite elements contain a defect density ρ_i, which traps carbon. These defects include dislocations and grain boundaries. Every defect is expected to trap a fraction from the abutting free-carbon. Since this proportionality is not known in the current literature regarding its possible dependence on the amount of the overall carbon concentration, we will assume a linear relationship (e.g. like Cottrell's model) in the whole range of carbon concentrations.

More specifically, the Cottrell model is only applicable for low carbon concentrations since it assumes that the trapped region corresponds only to the traction zone around defects (which is very small), whereas there is evidence that even in isolated dislocations the trapped region is much larger, e.g. 7–8 nm radius [30]. Atomistic simulations [15] which predict the 7–8 nm radius of segregation have shown that almost a constant proportionality remains even for much higher carbon concentrations than the ones dealt with by Cottrell. Therefore, we will assume a universal proportionality regardless of the amount of carbon, although this is a crude estimation.

For an elementary material unit i with defect density ρ_i, we can determine the trapped-carbon concentration $x_{C,i}^{trap}$ by assuming a proportionality also to ρ_i. This assumption is consistent with both types

---

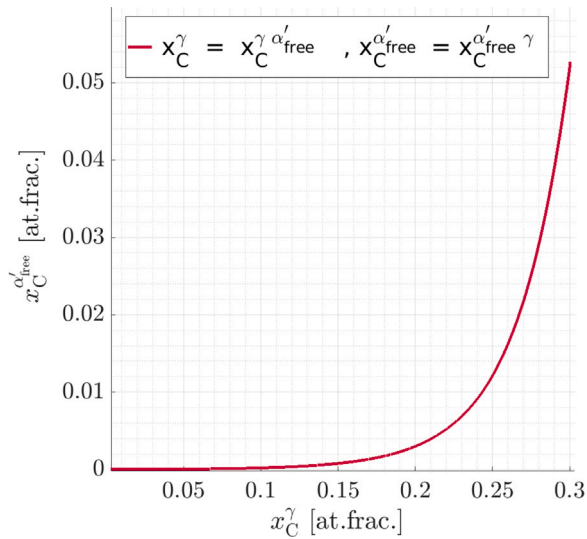[1] Note that it is straightforward to apply this model to 3D microstructures.

Fig. 1. Equilibrium carbon concentration values at 400 °C for adjacent α' and γ units satisfying $\mu_C^\gamma = \mu_C^{\alpha'_{\text{free}}}$.

of defects. More specifically, in the context of individual dislocations, their density multiplies the carbon concentration per dislocation, e. g. see [13,14]. Likewise, in the context of boundaries, the so-called enrichment ratio is also found to be proportional to the defect density [20].

Altogether, the local and temporal trapped-carbon concentration within the element i is determined as:

$$x_{C,i}^{\text{trap}} = k_C^{\text{defects}} \cdot \rho_i \cdot x_{C,i}^{\text{free}}. \tag{2}$$

The parameter k_C^{defects} [m^2] is constant and can be approximated based on the expected degree of trapping at defects in the quenched state. For example, in quenched Fe - 0.5 C wt.% martensite, Hutchinson et al. [21] found that around 96% of carbon is trapped. As the expected defect density for this carbon concentration is around $3.5 \cdot 10^{15}$ m^{-2} (a reasonable value based on [31–33]) in the present study we use $k_C^{\text{defects}} = 7 \cdot 10^{-15}$ m^2.

As indicated above, Eq. (2) will be used in the present work independently of the temperature. That is because the effects of temperature are rather unclear, e.g. some works [34,35] show high sensitivity to temperature, whereas in [15] a weak dependency is shown. Nevertheless, even if a temperature dependency is assumed, this would not be expected to be significant, since it would otherwise mean that the carbon concentration in the martensite solid solution increases significantly when heating from 25 °C to 400 °C.

2.2.3. Martensite–austenite interface partitioning

In the present study we assume an Fe-C material comprising either only martensite or martensite and austenite. The thermodynamic input for interphase partitioning at 400 °C is calculated for all possible local compositions, by setting equal the chemical potential of carbon in solid solution in γ and α' (i. e. α'_{free}), as calculated from Thermocalc using the TCFE13 database. The resultant relationship is shown in Fig. 1 and is applied locally in the numerical description in adjacent elementary units and per boundary. The subscript "free" refers to free carbon, hence indicating that only the carbon in solid solution in martensite partitions to austenite. The relationship plotted in Fig. 1 expresses the equilibrium concentrations $x_C^{\alpha'_{\text{free}}\gamma}$ and $x_C^{\gamma\alpha'_{\text{free}}}$, which are read as "carbon concentration in martensite solid solution in equilibrium with austenite", and "carbon concentration in austenite in equilibrium with martensite solid solution", respectively.

2.3. Global equilibrium

By definition the equilibrium distribution of carbon is reached when the chemical potential of carbon is equal everywhere. In the presence of defects in the martensite and two phases (α' and γ) this implies:

$$\mu_C^{\alpha'_{\text{free}}} = \mu_C^{\alpha'_{\text{trap}}} \tag{3a}$$

and

$$\mu_C^{\alpha'_{\text{free}}} = \mu_C^\gamma. \tag{3b}$$

The subscript "trap" refers to carbon trapped at defects. Since carbon segregation to defects in austenite is neglected, all carbon in austenite is free. Eq. (3) express that the carbon concentration in solid solution ("free") in martensite should be such that it is in equilibrium simultaneously with the carbon in the defect traps and in austenite.

Eq. (3a) amounts for the equilibrium concentrations of carbon in martensite, denoted by $x_C^{\alpha'_{\text{free}}\alpha'_{\text{trap}}}$ and $x_C^{\alpha'_{\text{trap}}\alpha'_{\text{free}}}$ for free and trapped, respectively, carbon in martensite. Eq. (3b) dictates the equilibrium concentrations of carbon in solid solution between the two phases, referred to as $x_C^{\alpha'_{\text{free}}\gamma}$ and $x_C^{\gamma\alpha'_{\text{free}}}$ for free carbon in martensite and free carbon in austenite, respectively. Hence, combining the solutions of Eq. (3a) and Eq. (3b) gives the equilibrium concentrations of carbon between the three lattice types we assume to constitute a martensite–austenite microstructure.

If the effects of carbon trapping at defects are not taken into account (i. e. $k_C^{\text{defects}} = 0$) the equilibrium state coincides with the Constrained Carbon Equilibrium (CCE) [10,36,37], since the expressions become equivalent to the assumption that the carbon solubility in martensite is equal to its solubility in ferrite. On the other hand, $k_C^{\text{defects}} \neq 0$ means that the equilibrium is reached when the free carbon obeys a martensite–austenite equilibrium, while the free carbon in the martensite is in equilibrium with the carbon in martensite defect traps (Eq. (3)). The equilibrium carbon concentrations together with mass conservation will then lead to:

$$x_C^{\alpha'_{\text{free}}\alpha'_{\text{trap}}} \cdot f^{\alpha'} + x_C^{\alpha'_{\text{trap}}\alpha'_{\text{free}}} \cdot f^{\alpha'} + x_C^{\gamma\alpha'_{\text{free}}} \cdot f^\gamma = x_0, \tag{4}$$

with x_0 the overall carbon concentration.

Given the defect density ρ in martensite, the mean-field expression (and equilibrium values) of Eq. (2) becomes

$$x_C^{\alpha'_{\text{trap}}\alpha'_{\text{free}}} = k_C^{\text{defects}} \cdot \rho \cdot x_C^{\alpha'_{\text{free}}\alpha'_{\text{trap}}}. \tag{5}$$

Given the martensite volume fraction $f^{\alpha'}$ and overall carbon x_0, Eqs. (4) and (5) and the relation of Fig. 1 give a unique solution, i. e. the equilibrium state.

Fig. 2 shows equilibrium solutions resulting from the approach we take in this model for martensite–austenite microstructures with varying austenite volume fractions, with the total carbon concentration equal to $x_0 = 0.0228$ at.fraction in all cases. It shows the results from the consideration of carbon trapping at defects with $k_C^{\text{defects}} = 7 \cdot 10^{-15}$ m^2, together with the case in which trapping is neglected, i. e. $k_C^{\text{defects}} = 0$. As stated before, for $k_C^{\text{defects}} = 0$ the equilibrium is the CCE. The arrows drawn in Fig. 2 indicate the deviation of the present model from the CCE.

Considering the experimental measurements reported for austenite enrichment, e. g. in [38–40], it is clear that the present approach predicts the carbon concentrations closer to the actual values, in comparison to the CCE. Discrepancies between the CCE predictions and experimental measurements are typically attributed to carbide formation [41]. However, here we show that the carbon trapped at martensite defects can also provide a physically valid reason for these deviations.

Furthermore, as is shown, decreasing the volume fraction of austenite results in equilibrium states that have carbon concentrations in austenite that differ more from the CCE. Oppositely, for example for $f^\gamma = 0.28$ the equilibrium is almost equal to the CCE. This observation is important because it explains why for example in Q&P steels
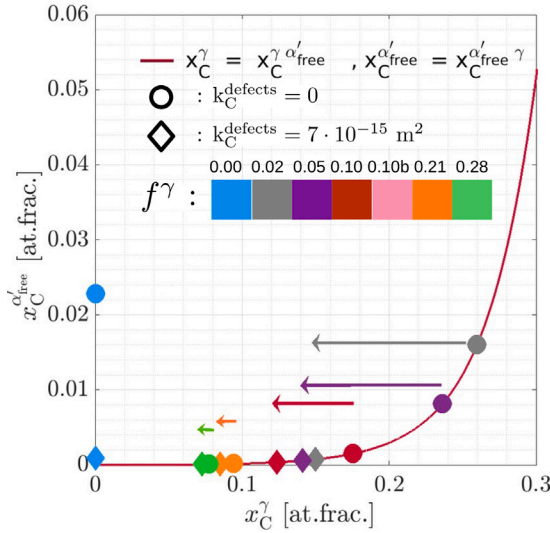
Fig. 2. Effect of phase fractions on the global equilibrium and comparison to the CCE. The equilibrium corresponds to a defect density in martensite equal to $3.5 \cdot 10^{15}$ m^{-2}, and overall carbon equal to $x_0 = 0.0228$ at.frac. Circular symbols correspond to the equilibrium by neglecting the segregation to defects, i.e. of austenite and martensite solid solution (CCE), and diamond symbols to the simultaneous equilibrium of carbon between austenite, martensite solid solution, and martensite defects. The arrows indicate the magnitude of carbon-trapping effects, and thereby also the deviation of the current model approach from the CCE.

partitioning leads indeed to high carbon enrichment of austenite [22], without this meaning that carbon trapping at martensite defects does not take place. Also, it has already been observed [38–40] that the CCE predictions are more applicable for higher austenite volume fractions. The predictions based on the present approach are in line with this trend. Therefore, the applicability of the CCE in high austenite fractions can be explained by the carbon trapped at martensite defects.

The physical interpretation of the phase fractions effects on the amount of carbon trapped at martensite defects is associated with carbon escaping the solid solution of martensite. Larger austenite fractions allow the martensite solid solution to relax from carbon, whereas decreasing the austenite fraction means that the martensite defects will have to serve this purpose, i.e. to host the carbon that the solid solution of martensite cannot accommodate.

2.4. Local equilibrium and kinetics

Although the mean field solution, i.e. global equilibrium, is well defined, it should be noted that the local development towards the equilibrium solutions described in Section 2.3 is not uniquely defined, meaning that the full field model has blurriness against the equilibrium concentrations of each phase. Specifically, the partitioning takes place in equal local phase fractions at phase boundaries, and the segregation to defects also takes place considering the local state variables (i.e. defect density and free carbon passing/existing). This is important since it enables the assessment of the kinetics and local aspects of carbon enrichment/depletion, especially since these depend on the local phase fractions, as will be shown later.

2.4.1. Chemical-potential equilibrium and governing kinetic expression
2.4.1.1. Local equilibrium. In a discrete space, for each elementary martensitic unit i the equilibrium between free and trapped carbon is instantaneously satisfied according to Eq. (2). For each pair of neighboring elements i and j one of two conditions applies: either the two phases are different or they are the same. In order to approach equilibrium, in the former case locally the partitioning of carbon between α' and γ takes place across the ij boundary. In the latter

case only the concentration-gradient diffusion-related driving force described by Fick [29] acts, considering also the simultaneous satisfaction of trapped-to-free ratio (Eq. (5)) if the neighbor material elements are martensite.

An example of the local equilibrium is shown in Fig. 3, which shows five material elements: four α' elements, sharing the green boundaries, and one γ element, sharing the orange boundary with an α' element. The ratio $x_{C}^{\alpha'_{trap}}/x_{C}^{\alpha'_{free}}$ according to Eq. (2) is indicated in each α' element.

Eq. (6) shows the expressions describing the equilibrium between neighboring α' and γ elements, i.e. i and k in Fig. 3.

$$
\left.
\begin{array}{l}
\textbf{Orange boundary in Fig. 3}(\alpha'/\gamma) \\[4pt]
\text{(a) trapped and free equilibrium in } i: \\[4pt]
x_{C,i}^{tot} = (k_C^{defects} \cdot \rho_i + 1) \cdot x_{C,i}^{\alpha'_{free}} \\[4pt]
\text{(b) } ik \text{ phase equilibrium:} \\[4pt]
x_{C,i}^{\alpha'_{free}} = \left(x_C^{\alpha'_{free}\gamma} \right)_{ik} ; \; x_{C,k}^{\gamma} = \left(x_C^{\gamma\alpha'_{free}} \right)_{ki} \\[4pt]
\text{(c) } i \text{ and } k \text{ mass conservation:} \\[4pt]
x_{C,i}^{tot} + x_{C,k}^{tot} = f(x_C^{tot})
\end{array}
\right\}
\tag{6}
$$

In Eq. (6), $\left(x_C^{\alpha'_{free}\gamma} \right)_{ik}$ and $\left(x_C^{\gamma\alpha'_{free}} \right)_{ki}$ are used to refer to the equilibrium between the infinitesimal region of elements i and k at the phase boundary.

Eq. (7) shows the equations describing the equilibrium between two adjacent α' elements, e.g. i and j (elements separated by a green boundary) in Fig. 3.

$$
\left.
\begin{array}{l}
\textbf{Green boundaries in Fig. 3}(\alpha'/\alpha') \\[4pt]
\text{(a) trapped and free equilibrium at } i: \\[4pt]
x_{C,i}^{tot} = (k_C^{defects} \cdot \rho_i + 1) \cdot x_{C,i}^{\alpha'_{free}} \\[4pt]
\text{(b) trapped and free equilibrium at } j: \\[4pt]
x_{C,j}^{tot} = (k_C^{defects} \cdot \rho_j + 1) \cdot x_{C,j}^{\alpha'_{free}} \\[4pt]
\text{(c) } i \text{ and } j \text{ concentration gradient:} \\[4pt]
x_{C,i}^{\alpha'_{free}} - x_{C,j}^{\alpha'_{free}} = f(D_{ij}, \delta t, \delta z) \\[4pt]
\text{(d) } i \text{ and } j \text{ mass conservation:} \\[4pt]
x_{C,i}^{tot} + x_{C,j}^{tot} = f(x_C^{tot})
\end{array}
\right\}
\tag{7}
$$

where δt is the time step, D_{ij} is the carbon diffusivity between i and j and δz their distance. The local equilibrium for each pair of neighboring elements in Fig. 3 and expressed in Eqs. (6) and (7) applies to the overall regime describing element i. However, as suggested by Eq. (6)(c) and Eq. (7)(d), the local equilibrium of a cell with its neighborhood is not independent from the neighboring cells' equilibrium with their own surroundings. In other words, the actual local and temporal evolution is computed numerically, i.e. under the long-range diffusion related to the solid solution concentration gradients arising from concentration differences, due to interphase partitioning and trapping at defects as expressed in Eq. (7)(c).

2.4.1.2. Kinetics. The mass transport due to concentration gradients in solid solution, explained by Fick [29], follows:

$$
\frac{\partial x_{C,i}^{free}}{\partial t} = \bar{D}_i \cdot \frac{\partial^2 x_{C,i}^{free}}{\partial \bar{z}^2} \quad \forall \; i
\tag{8}
$$

where $\bar{D}_i$ is the diffusivity matrix (all neighboring elements) of carbon in element i and its same-phase neighbors located at $d\bar{z}$ from i, with $d\bar{z}$ the location vector between neighboring elements.

The diffusivity matrix in Eq. (8) is calculated at each simulation step as it comprises elements $D_{ij} = 1/2 \cdot D_i + 1/2 \cdot D_j$, i.e. the carbon diffusivity for mass transport between i and j.
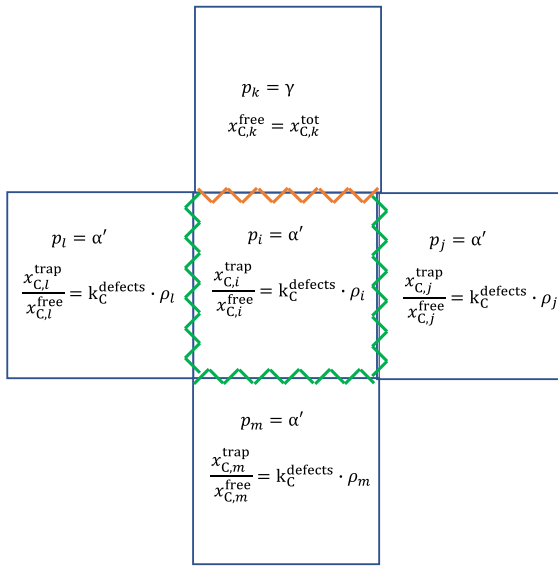
Fig. 3. Schematic of the local equilibrium between a cell i and its neighborhood based on the present approach. (For interpretation of the references to color in this figure legend, the reader is referred to the web version of this article.)

The numerical expression of Eq. (8), which considers the kinetics towards local equilibrium based on finite differences (under the consideration of Eqs. (6) and (7)), is

$$\frac{1}{1 + k_C^{\text{defects}} \cdot \rho_i} \cdot \left(x_{C,i}^{\text{tot},n+1} - x_{C,i}^{\text{tot},n} \right) =$$

$$\sum_j^{p_i = p_j}{}' \left(A_{ij} \cdot \left(\frac{1}{1 + k_C^{\text{defects}} \cdot \rho_j} \cdot x_{C,j}^{\text{tot},n} - \frac{1}{1 + k_C^{\text{defects}} \cdot \rho_i} \cdot x_{C,i}^{\text{tot},n} \right) \right) + \tag{9}$$

$$\sum_j^{p_i \neq p_j} \left(A_{ij} \cdot \left(\frac{1}{1 + k_C^{\text{defects}} \cdot \rho_i} \cdot x_{C,i}^{\text{tot},n} - x_{C,i}^{p_i p_j,n} \right) \right)$$

where

- j is the index indicating that element j is a same-phase ($p_i = p_j$) or different-phase ($p_i \neq p_j$) neighbor to element i;
- $A_{ij} = D_{ij} \cdot \frac{\delta t}{\delta z^2}$ is the rate factor that locally depends on the phase;
- n is the iteration step;
- $x_{C,i}^{p_i p_j,n}$ is $\left(x_C^{\alpha'_{\text{free}} \gamma} \right)_{ij}$ if element i is α' and element j is γ and $\left(x_C^{\gamma \alpha'_{\text{free}}} \right)_{ji}$ in the opposite case.

The different-phase equilibrium at the interface is satisfied by interface partitioning, which is calculated locally (i.e. for 50% α' and 50% for γ). It changes per iteration step n, as the carbon concentration at the interface depends on the nth solution of the carbon concentration in elements i and j. More precisely, we have

$$x_{C,i}^{\text{eq},n} = f\left(\frac{1}{2} x_{C,i}^{\text{free},n} + \frac{1}{2} x_{C,j}^{\text{free},n} \right), \tag{10}$$

where f is the phase equilibrium relation shown earlier in Fig. 1.

The algorithm's steps and numerical solvers are explained in section A1 of the supplementary material. After convergence the simulated time is increased with a time step δt. The sensitivity of the simulation to the time step δt in view of the present model assumptions is studied and shown in the supplementary material (section A2). The dependency on the grid settings is extremely small, which is expected since all additions (carbon partitioning, carbon trapping) are part of the numerical system for carbon diffusion (i. e. they are also solved in every iteration).

Regarding the diffusivity of carbon, the relationships selected here are taken from [42], [43], for $T = 400$ °C, which is the temperature

in all simulations in the present study. However, for the concentration-dependent diffusivity in austenite [43], a constant effective value was used in all simulations in order to avoid very small time steps. It is shown that the effect of the diffusivity of carbon in austenite on the evolution of carbon rejection from martensite and carbon trapping is minor (see section A3 in the supplementary material). In all simulations the diffusivity in austenite is taken equal to the one proposed by Ågren [43] for $x_{C,i}^\gamma = 0.15$ at. fraction, which is an intermediate value found in all simulations. The applied values of the carbon diffusivity at 400 °C are $6.1 \cdot 10^{-13}$ m^2/s for α' and $8.2 \cdot 10^{-14}$ m^2/s for γ.

The model is implemented in CASIPT (cellular automata sharp-interface model for phase transformations) [44–47] and in the open source program OMicroN (optimizing microstructures numerically) [46].

2.4.2. Artificial bicrystal

This subsection shows the simulation process by using the example of an artificial bicrystal. As is shown in Fig. 4, the artificial microstructure consists of a circular austenite grain within a martensite grain. The martensite grain contains a dislocation density ρ_i that varies; the vertical strips have $\rho_i = 1 \cdot 10^{15}$ m^{-2} or $\rho = 5 \cdot 10^{15}$ m^{-2}, while the remaining martensite has $\rho = 0$.

Fig. 5 shows the simulated carbon redistribution from the initial, quenched state up to 100 s annealing at 400 °C. As shown in Fig. 5a, the starting total carbon concentration is 0.0228 at.fraction in both phases. Fig. 5c and Fig. 5e show that in the dislocation-containing regions of martensite carbon is partly trapped and the free-carbon concentration is smaller than the overall carbon concentration.

Carbon diffuses from martensite to austenite, as well as from the dislocation-free or -poor areas to the dislocation-rich areas. This increases the trapped and total carbon concentration in the dislocation-rich areas (Fig. 5b and Fig. 5d). This effect is strongest in the areas at a certain distance from the austenite grain, since the solid-solution concentration gradients due to austenite enrichment are still far from equilibrium. All this is realized by the mesoscale free-carbon concentration gradients, which as shown in Fig. 5f for martensite and in Fig. 5b for austenite gradually weaken in the individual phases. Since the carbon diffusivity in austenite is lower than in martensite, after 100 s at 400 °C a concentration gradient is still more pronounced in austenite. The diffusion length $\sqrt{Dt}$ for carbon is 7.8 μm in martensite and 2.8 μm in austenite.

Another feature is that, initially, the trapped-carbon concentration was very high – and almost equal – inside all the strips, despite the fact that some strips contain five time higher defect density than others. But during annealing, mostly the dislocation-rich strips trap carbon. This is because, initially, the free carbon in martensite is not in equilibrium, since mesoscale diffusion has not taken place. Annealing eliminates the solid-solution concentration gradients, and thus the trapped-carbon concentration varies proportionally to the defect density.

Finally, the carbon enrichment of the dislocation-rich regions away from austenite is so high that it exceeds the carbon concentration in austenite — as shown in Fig. 5b. This is of course a temporal phenomenon; the global equilibrium concentrations are such that the carbon concentration at martensite defects is lower than in austenite. This phenomenon occurs due to these dislocation-rich areas being surrounded by dislocation-free and dislocation-poor regions that reject their carbon. Since the latter are still unaffected by the carbon-depletion due to phase partitioning, their carbon diffuses towards the abutting dislocation-high regions. This is more clearly seen in the bottom row of Fig. 5 where it is clear that the free-carbon concentration in the strips, which was once low (Fig. 5e), becomes similar to the one in the surrounding martensite (Fig. 5f).

2.4.3. Experimental microstructures

In total seven experimental microstructures of different features were used as input in the simulations. Six differ in the fraction of
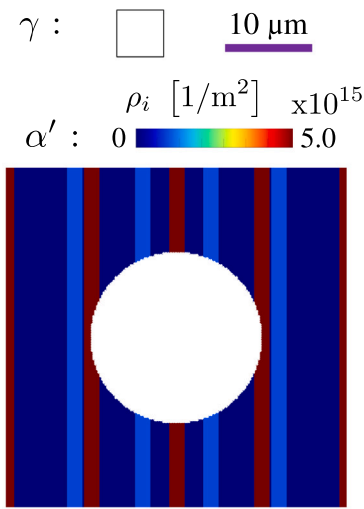
Fig. 4. Bicrystal example with artificial variations in the dislocation density ρ_i; The map shows the phase (colored white if γ) and martensite dislocation density.

retained austenite (varying from 0 to 0.28) and one exhibits a banded structure, with an austenite fraction $f^\gamma = 0.10$.

All microstructures, hereafter referred to as RVE (Representative Volume Element), were experimentally obtained by EBSD. Each RVE encompasses an area of 80×80 μm^2 and is resolved by elements of area 0.2×0.2 μm^2. The measured data were not filtered; non-indexed pixels were assigned the orientation of the (randomly chosen) nearest indexed pixel, instead.

The EBSD maps come from measurements of different Q&P-processed materials. These EBSD maps are used only as model microstructures to investigate the model outcomes. Specifically, the above-mentioned areas were extracted depending on the austenite fraction and/or distribution in order to obtain, and compare through the simulations, RVEs of different phase distributions.

The defect concentration in martensite is determined from the local crystallographic orientations, measured by EBSD. For each martensitic element i the average misorientation θ_i with its martensitic neighboring elements is calculated, in which for the misorientation across high-angle grain boundaries a fixed value of 7° is taken. It is generally accepted that the misorientation within a grain can be related with the density of geometrically necessary dislocations. In this model, the defect density ρ_i in each element is taken proportional to its average misorientation [48]. The defect density is the combined density of grain boundaries and dislocations, which can both act as carbon traps. In the present model, the defect density is given the unit m^{-2}, in line with the dislocation density.

To enable a consistent comparison in the different outcomes, the local misorientation θ_i in martensite was translated by linear scaling to a defect density $\rho_i^{\alpha'}$, such that the average density in martensitic elements is equal to $3.5 \cdot 10^{15} m^{-2}$. The latter value was chosen approximately based on existing models [31–33] for quenched Fe - 0.0228 C (at. fraction) martensite. The defect-density distributions are shown in Fig. 6.

As is shown, despite the different austenite fractions, the defect-density distribution is set similarly in all model microstructures. Therefore, the simulated outcomes and comparisons can be directly related to the RVEs' differences in the austenite fraction.

3. Results and discussion

3.1. Carbon redistribution in a fully martensitic microstructure

Fig. 7 shows the simulated carbon redistribution in a fully martensitic structure during annealing at 400 °C for 300 s. Regarding the
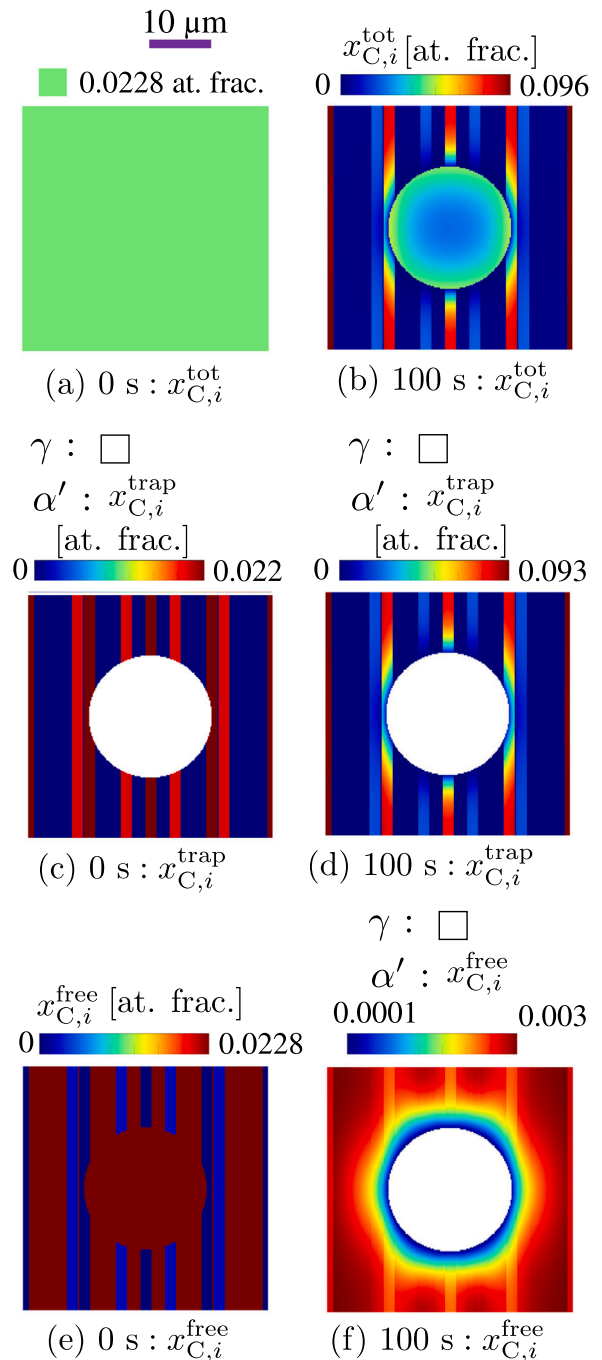

Fig. 5. Simulation example at 400 °C; (a), (b) show the total carbon concentration at 0 s and 100 s, respectively, (c), (d) show the carbon concentration that is trapped at 0 s and 100 s, respectively, (e), (f) show the free-carbon concentration (solid solution) at 0 s and 100 s, respectively.

behavior towards global equilibrium, it becomes clear that while initially martensite traps carbon almost everywhere, despite spatial differences in the trap density (e. g. boundary vs. bulk), annealing results in a pronounced enrichment, mostly at boundaries, while decreasing the carbon concentration in bulk martensite. The reason for this was explained earlier in Section 2.4.2. The physical interpretation of this phenomenon becomes clear here, since austenite is absent. Initially, carbon in martensite cannot undergo long range diffusion. i.e. the total carbon concentration is equal everywhere, and hence makes use of the available defects wherever possible, regardless of their density. During annealing, even if austenite is not present, carbon makes use of each
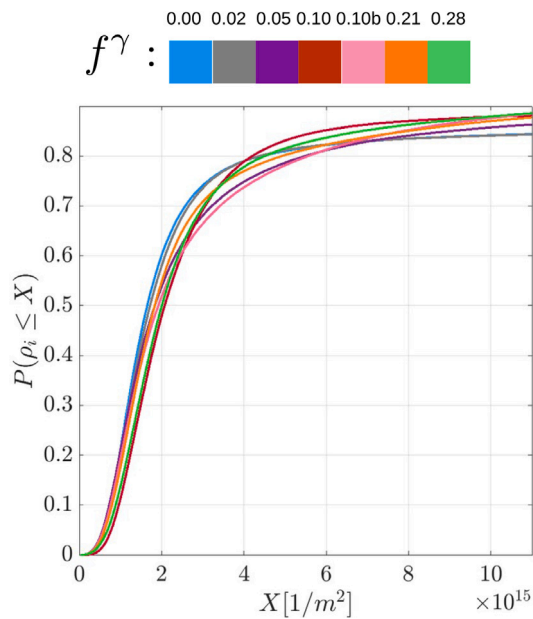
Fig. 6. Cumulative distributions of the martensite defect density corresponding to each one of the seven microstructures used in the present investigation. The $f^\gamma = 0.10\text{b}$ refers to the banded microstructure of 10% austenite.

Fig. 8. Martensite–austenite microstructure ($f^\gamma = 0.10$) obtained by EBSD. The map shows the phase (colored white if austenite) and defect density (if martensite).
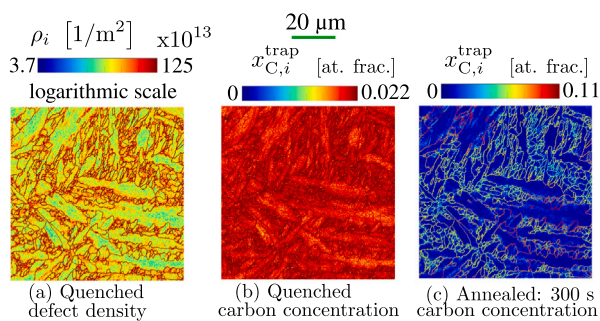

Fig. 7. Simulated trapped-carbon concentration in a 100 % martensitic microstructure; (a) at the quenched state and (b) after 300 s of annealing at 400 °C. (For interpretation of the references to color in this figure legend, the reader is referred to the web version of this article.)

3.2. Carbon redistribution in martensite–austenite microstructures

3.2.1. Redistribution of carbon

Simulations on carbon redistribution have been performed for the six martensite–austenite microstructures presented in Section 2.4.3. As a first example, the annealing simulation of an austenite–martensite microstructure containing 10% austenite is discussed. The spatial distribution of defects is shown in Fig. 8.

Fig. 9 shows the spatially resolved carbon-concentration related variables; (a), (c), (e) give the initial distribution of total, trapped- and free-carbon concentration, respectively. During 300 s of annealing at 400 °C the carbon partitions from martensite to austenite, as is evident from Fig. 9b. Fig. 9d shows that the trapped carbon redistributes such that most martensite units are alleviated from carbon due to segregation to defects, most strongly to lath boundaries, where the defect density is highest. For instance, the dark-blue regions in Fig. 9d have a trapped-carbon concentration less than 0.01 at. fraction, whereas these regions have a concentration of around 0.02 at. fraction in the initial condition (orange/red in Fig. 9c). The free-carbon concentration gradients in both phases diminish (Fig. 9f), although there are distinct differences in the carbon concentrations in different austenite grains. These differences are caused by the different amounts of carbon that each grain could absorb from its surroundings. There is a distinct tendency of the smaller austenite grains having a higher carbon concentration.

Regarding the local and temporal carbon redistribution in martensite–austenite microstructures, here the evolution is more complex than the uniform case of a simple bicrystal discussed in Section 2.4.2. In the latter case only martensitic regions far from austenite temporarily increase the trapped-carbon concentration. However, here also other martensitic locations attract carbon and preserve considerable concentrations throughout the annealing. Specifically, martensite traps carbon not only when it is far from austenite, but also when it is very close to austenite grains. This is found in martensite abutting very small austenite grains or when found in regions of smaller fraction compared to the average retained austenite fraction. In such cases, the carbon flux towards austenite leads to a related degree of carbon trapping at defects, because partitioning in these regions is yet far from global equilibrium, meaning that there is more martensite to enrich austenite and the adjacent traps absorb high amounts of carbon.

The temporal phenomena of carbon trapping and de-trapping are more clear in Fig. 10. Here, the spatial evolution of the trapped-carbon

defect equally, and thus the trapped-carbon concentration becomes proportional to the defect density.

As for the local and temporal behavior (before equilibrium), the simulations show that martensite primarily enriches in carbon concentration at boundaries surrounding large laths. The boundaries of large laths have a reddish color, which implies an enrichment up to around 0.10 at. fraction, whereas the boundaries of many small laths have a trapped-carbon concentration of typically 0.03 at. fraction (light blue in Fig. 7(c). The reasons for this phenomenon are two. Firstly, regions of high density of defect traps (lath boundaries) will attract the carbon from surrounding defect-poor regions, and thus the larger the lath, the more carbon is available for transport into the boundaries. Secondly, larger blocks contain lower defect densities in the interior, as shown in Fig. 7(a) and in [49], which forms an additional reason (compared to smaller laths/blocks) for carbon to escape and diffuse towards the boundaries.

Altogether, even in a fully martensitic microstructure, carbon trapping at defects during annealing evolves differently from the prior quenched state. In terms of equilibrium, carbon enrichment is proportional to their defect density. In terms of temporal state (i.e. non-equilibrium) large lath size boundaries are mostly enriched.
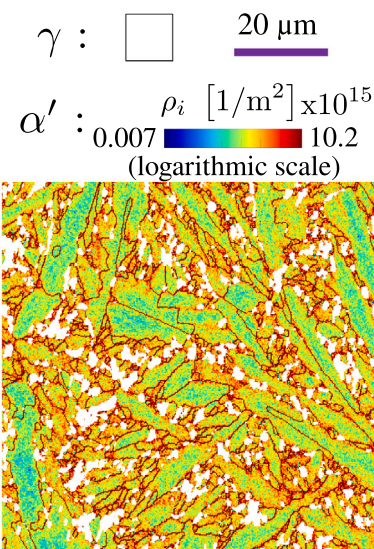
$$x^{\text{tot}}_{\text{C},i} \text{ [at. frac.]}$$
0 — 0.16

(a) 0 s : $x^{\text{tot}}_{\text{C},i}$

(b) 300 s : $x^{\text{tot}}_{\text{C},i}$

$\gamma : \square$
$\alpha' : x^{\text{trap}}_{\text{C},i}$
[at. frac.]
0 — 0.022

$\gamma : \square$
$\alpha' : x^{\text{trap}}_{\text{C},i}$
[at. frac.]
0 — 0.09

(c) 0 s : $x^{\text{trap}}_{\text{C},i}$

(d) 300 s : $x^{\text{trap}}_{\text{C},i}$

$x^{\text{free}}_{\text{C},i}$ [at. frac.]
0 — 0.0228

$x^{\text{free}}_{\text{C},i}$ [at. frac.]
0 — 0.16

(e) 0 s : $x^{\text{free}}_{\text{C},i}$

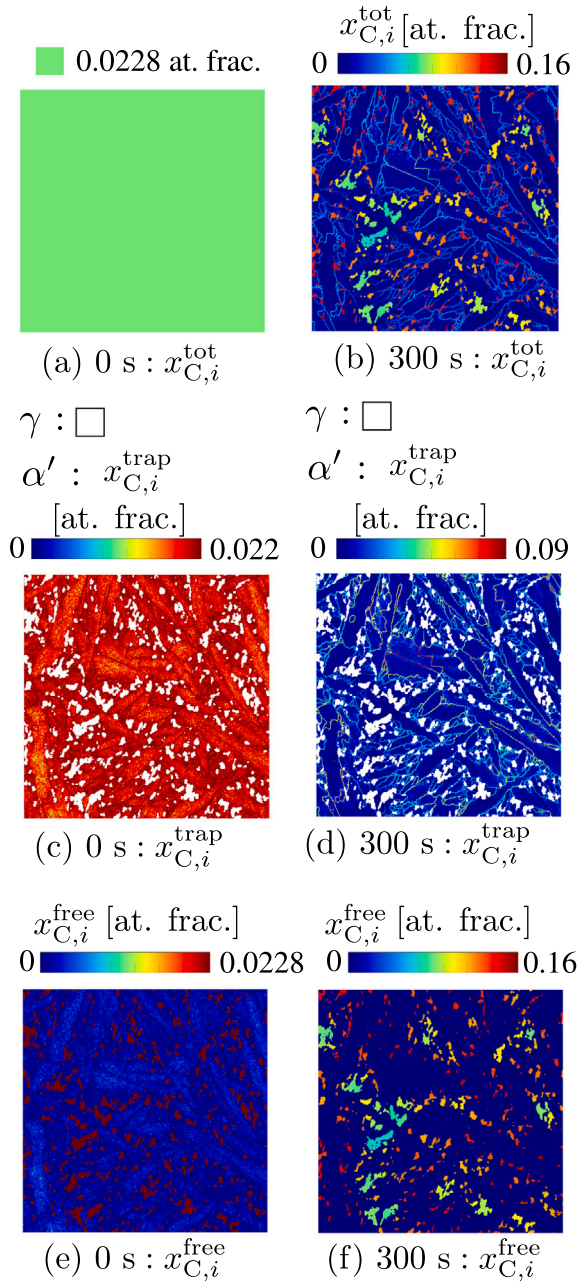(f) 300 s : $x^{\text{free}}_{\text{C},i}$

Fig. 9. Simulation of annealing at 400 °C a martensite–austenite microstructure ($f^\gamma = 0.10$); (a), (b) show the total carbon concentration at 0 s and 300 s, respectively, (c), (d) show the trapped-carbon concentration at 0 s and 300 s, respectively, (e), (f) show the free-carbon concentration at 0 s and 300 s, respectively.

concentration is shown in comparison to the initial quenched state, i. e. $\delta x^{\text{trap}}_{\text{C},i} = x^{\text{trap}}_{\text{C},i}(t) - x^{\text{trap}}_{\text{C},i}(0)$, where t is the annealing time, indicated in the figure.

By comparing the maps in the zoomed-in area in Fig. 10, it is shown that in the early stages of annealing (50 s) most carbon diffuses to and becomes trapped at the boundaries at a certain distance from austenite (for instance the boundary indicated by the pink arrow in Fig. 10(a)), whereas the martensitic defects close to austenite actually exhibit a decrease in the carbon concentration (the region indicated by the green arrow). In the later stages the latter regions show a trend reversal, where now some boundaries next to austenite increase the trapped-carbon concentration. Hence, now the maximum trapped-carbon concentration pertains to martensite either far from austenite or close to small austenite grains.
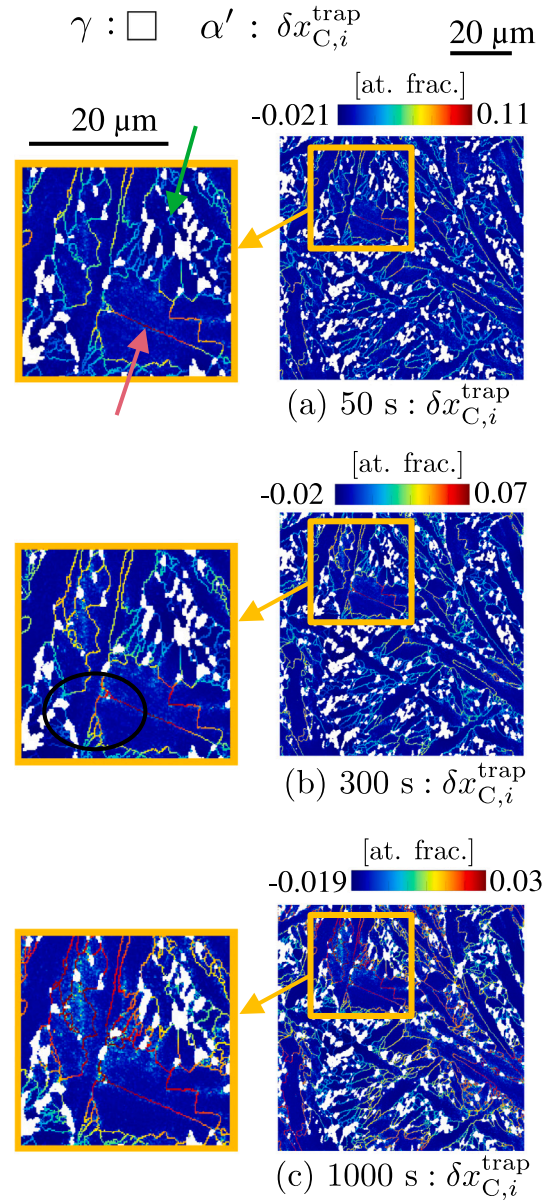

$\gamma : \square$ $\alpha' : \delta x^{\text{trap}}_{\text{C},i}$ 20 μm

[at. frac.]
-0.021 — 0.11

20 μm

(a) 50 s : $\delta x^{\text{trap}}_{\text{C},i}$

[at. frac.]
-0.02 — 0.07

(b) 300 s : $\delta x^{\text{trap}}_{\text{C},i}$

[at. frac.]
-0.019 — 0.03

(c) 1000 s : $\delta x^{\text{trap}}_{\text{C},i}$

Fig. 10. Changes in trapped-carbon concentrations during annealing of a martensite/austenite microstructure ($f^\gamma = 0.10$). The difference between the trapped-carbon concentration at time t and in the initial state $\delta x^{\text{trap}}_{\text{C},i} = x^{\text{trap}}_{\text{C},i}(t) - x^{\text{trap}}_{\text{C},i}(0)$ is shown after: (a) $t = 50$ s and (b) $t = 300$ s and (c) $t = 1000$ s of annealing at 400 °C.

These trends comply with experimental observations of Yuan et al. [7], who find that during the early stages of annealing of martensite/austenite microstructures, carbon clustering at defects and thenceforth also carbide formation was only observed in martensitic defects either at a distance from austenite (e. g. some lath boundaries) or very close to austenite.

Some lath boundaries at a distance from austenite contain around up to 0.11 at.fraction trapped carbon, which is a concentration that favors the nucleation of carbides [35]. On the other hand, the enriched martensite/austenite interfaces, mostly the ones surrounding small austenite grains, would probably migrate into martensite, in agreement with the local equilibrium [50]. The high localization of carbon near the newly formed or pre-existing austenite/martensite interfaces can lead to interface motion, as explained by Santofimia et al. [11]. In this view, and considering also the high localized carbon concentrations simulated in the present approach, austenite growth can be expected. This phenomenon was also observed by Yuan et al. [7]
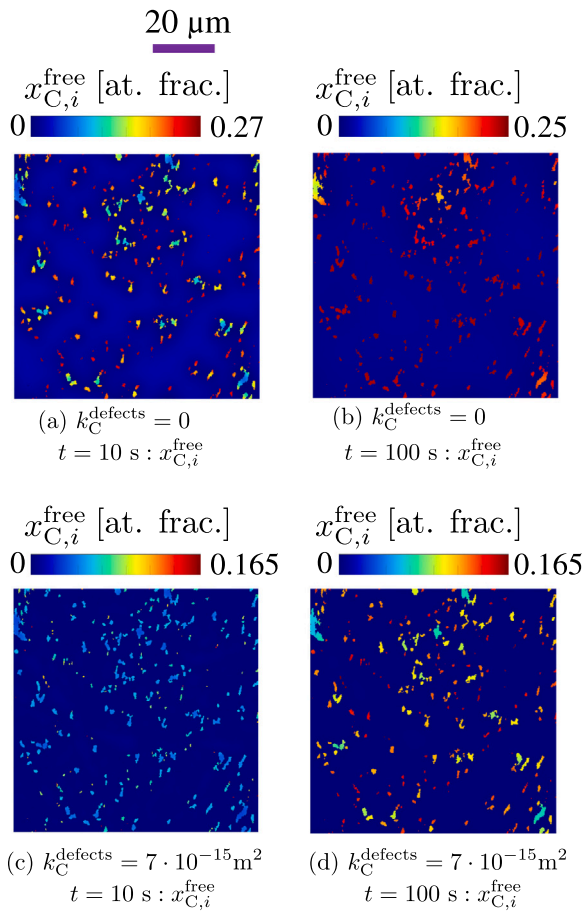
(a) $k_C^{\text{defects}} = 0$
$t = 10$ s : $x_{C,i}^{\text{free}}$

(b) $k_C^{\text{defects}} = 0$
$t = 100$ s : $x_{C,i}^{\text{free}}$

(c) $k_C^{\text{defects}} = 7 \cdot 10^{-15} \text{m}^2$
$t = 10$ s : $x_{C,i}^{\text{free}}$

(d) $k_C^{\text{defects}} = 7 \cdot 10^{-15} \text{m}^2$
$t = 100$ s : $x_{C,i}^{\text{free}}$

Fig. 11. Simulations of annealing at 400 °C with and without the consideration of trapping to defects, for a microstructure with $f^\gamma = 0.05$.

Fig. 12. Simulations of annealing at 400 °C with and without the consideration of trapping at defects, for a microstructure with $f^\gamma = 0.05$. The asterisks indicate the half-times $t_{1/2}$.

insofar as the austenite fraction doubled in less than two minutes at 400 °C, regardless of the phase fractions in the global equilibrium.

3.2.2. Effects on austenite enrichment

This subsection investigates the effects of carbon trapping at defects on carbon enrichment of austenite, using a microstructure with $f^\gamma = 0.05$. Fig. 11 shows the free-carbon concentration maps after annealing at 400 °C for $t = 10$ s and $t = 100$ s, simulated with defect trapping ($k_C^{\text{defects}} = 7 \cdot 10^{-15}$ m^2) and without ($k_C^{\text{defects}} = 0$). The simulations show that carbon trapping at defects in martensite significantly slows down the carbon enrichment of austenite. The rapid austenite enrichment (i.e. already up to $x_C^\gamma = 0.25$ at. fraction in small grains after 10 s) revealed by the simulation that does not account for carbon trapping differs significantly from the case where trapping is considered. In particular, the simulation accounting for trapping shows many light-blue austenite grains after 10 s ($x_C^\gamma \approx 0.05$ at. fraction) and yellowish grains after 100 s ($x_C^\gamma \approx 0.11$ at. fraction). For the simulations in which carbon trapping is not considered the typical concentrations in austenite after 10 s and 100 s are 0.09 – 0.21 at. fraction and 0.21 – 0.27 at. fraction, respectively.

The delay in carbon enrichment of the austenite due to carbon trapping at martensite defects is also clearly reflected in the overall carbon concentration in austenite as a function of time, shown in Fig. 12. This figure shows that the eventual equilibrium carbon concentration in austenite ($x_{C,eq}^\gamma$) is distinctly lower due to carbon trapping in martensite, which lowers the free-carbon concentration in martensite, with which the free-carbon concentration in austenite reaches equilibrium. In addition, it requires more time for the carbon concentration to converge to the equilibrium value when martensite-defect trapping is considered. Specifically, the half-time $t_{1/2}$, i.e. the
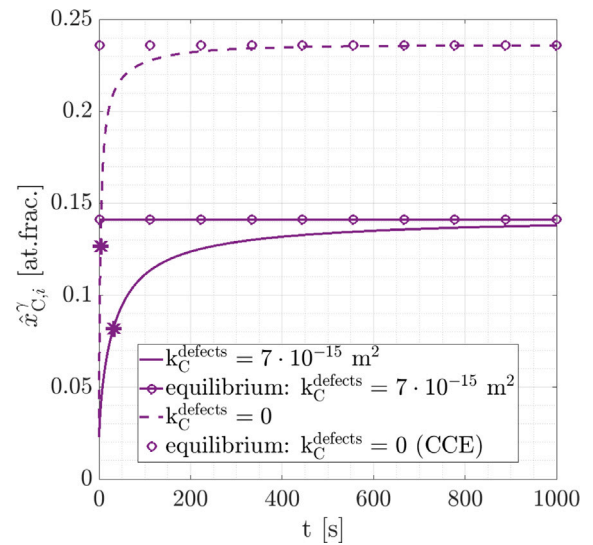
time required to reach the carbon concentration $\frac{1}{2}\left(x_{C,eq}^\gamma - x_C^\gamma(t = 0)\right)$ (see asterisks on the curves of Fig. 12) is around 3 s without and 31 s with the effect of carbon trapping at defects.

3.3. Effects of microstructural aspects on carbon segregation to defects

3.3.1. Influence of austenite fraction

Fig. 13 shows the overall time evolution of the trapped-carbon concentration in martensite and the carbon concentration in austenite for microstructures of different phase fractions. The kinetics of the associated processes are again quantified based on half-time $t_{1/2}$, indicated with an asterisk in the figures. The de-trapping of carbon in martensite is an indirect consequence of carbon partitioning from martensite to austenite, which lowers the free-carbon concentration in martensite. The trapped-carbon concentration is then affected through Eq. (2).

Fig. 13a shows that the relative carbon de-trapping rate is higher for larger austenite fractions. This trend is associated with the higher density of martensite/austenite interfaces, which facilitates carbon partitioning, and smaller diffusion distances for the carbon within martensite to reach an interface with austenite.

The austenite enrichment shows an increase in $t_{1/2}$ for increasing austenite fraction up to $f^\gamma = 0.10$, but a decrease for larger austenite fractions. This non-monotonous trend is due to the combination of two effects. One is the fact that carbon is to be distributed over a larger volume of austenite with increasing fraction, which makes the process slower. The second effect is the lower equilibrium carbon concentration for higher austenite fractions, which makes the relative enrichment rate higher.

3.3.2. Influence of microstructure banding

This subsection investigates the effects of spatial heterogeneity of the phase distribution on the carbon partitioning and trapping, beyond the extent of the effects that the topology has on the diffusion itself. We compare two microstructures with the same phase fractions ($f^\gamma = 0.10$), but with a different degree of spatial heterogeneity: one with a relatively homogeneous microstructure and one with pronounced local variations in phase fractions inherent to e. g. chemical segregation (banding).

The difference between the two RVEs in the spatial heterogeneity of austenite and martensite is confirmed by separating the RVEs into 25 areas and quantifying the phase fraction in each area, as indicated
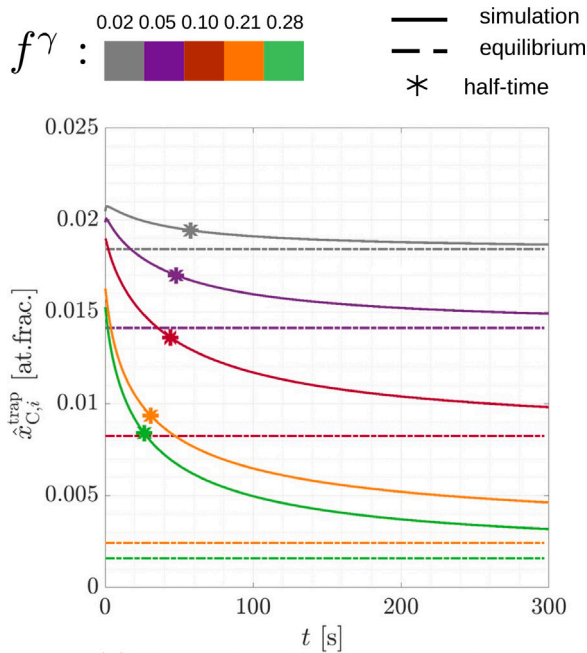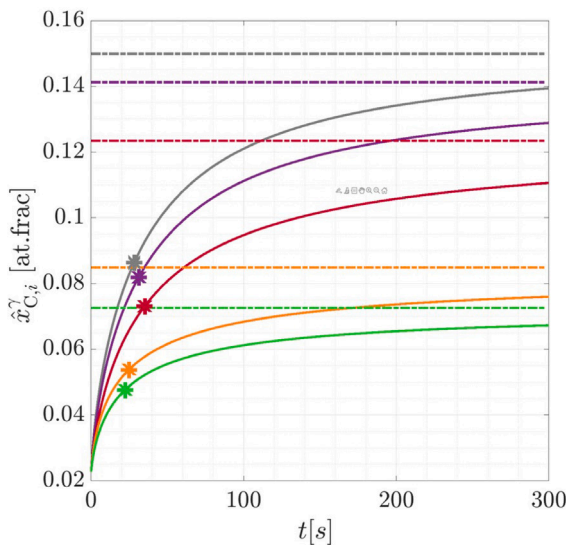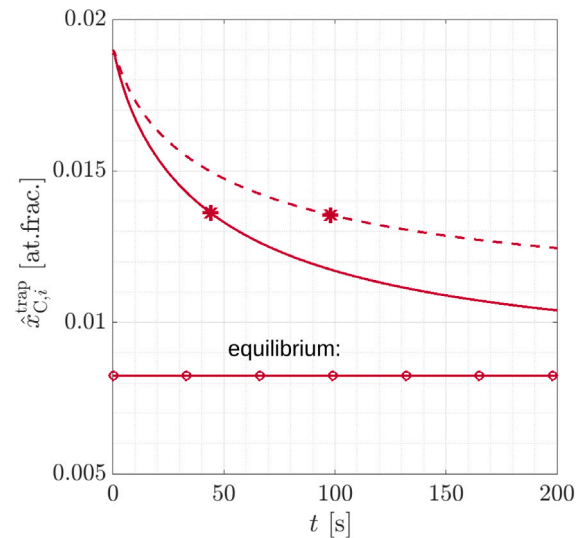
Fig. 13. Time evolution of carbon concentration redistribution; (a) shows the average carbon concentration in martensite defects and (b) the average carbon concentration in austenite, for simulations of annealing at 400 °C under the consideration of trapping to defects, for the microstructures of different austenite fraction. The asterisks indicate the half-life times $t_{1/2}$.

Fig. 14. Simulated outcome of average carbon concentration (a) segregated to martensite defects, and (b) in austenite, during annealing at 400 °C for different microstructures of the same austenite fraction; The asterisks indicate the half-times, namely (a) the de-trapping 44 s and 98 s, and (b) the austenite enrichment 35 s and 66 s, for the homogeneous and heterogeneous microstructure, respectively.
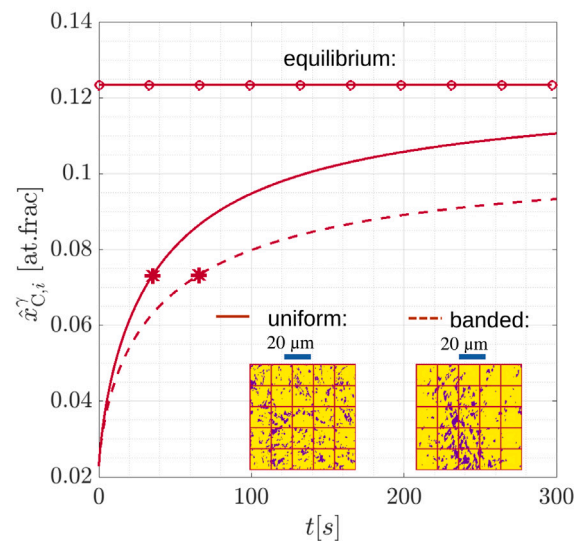
by the legend of Fig. 14. The width of the phase-fraction distribution in the first RVE is 0.03, whereas the second has a width of 0.10.

The effect of topological heterogeneities on austenite distribution in martensite in the overall process of carbon de-trapping is shown in Fig. 14. It is clear that increasing the degree of spatial heterogeneity significantly delays the process of carbon de-trapping and thereby austenite enrichment.

The main difference causing the delay in the de-trapping process, and thus also in the enrichment of austenite, is explained by the top row images in Fig. 15. The pink colored pixels have carbon concentration trapped more than 0.003 at. fraction, which is an arbitrarily chosen value. Annealing the homogeneous RVE results in a similar behavior of carbon trapping throughout the microstructure, as indicated by the

uniformly distributed pink colored pixels in the top row of Fig. 15a. However, the banded microstructure gives a heterogeneous behavior, where the pink martensite pixels are concentrated in the middle. Essentially, the middle region contains a higher austenite fraction in comparison to the whole RVE. Hence, most carbon is partitioned into austenite in the center, while regions further away are exempted from supplying carbon to austenite. This is why it requires more time for the heterogeneous microstructure to reach equilibrium.

The effect of banding in austenite enrichment is shown in the bottom row images of Fig. 15. Martensite is colored black. The pink- and green-colored pixels contain more, and less respectively, carbon than the equilibrium concentration. It is clear that even after 300 s of annealing the carbon enrichment is still heterogeneous in the banded microstructure. The uniform RVE has austenite sites that are more enriched (pink pixels in bottom image Fig. 15a) or less enriched (green pixels in bottom image Fig. 15a), in comparison to the thermodynamic
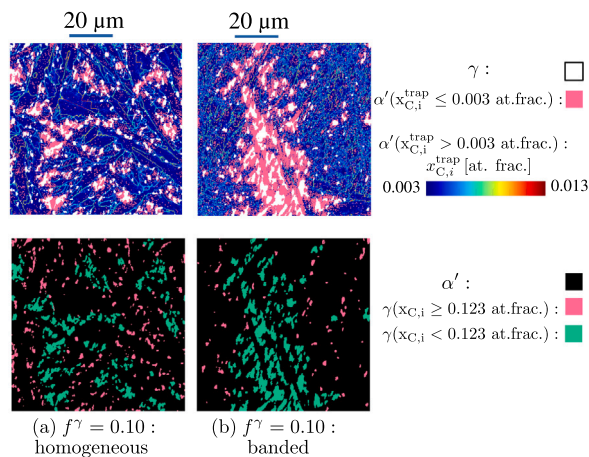
Fig. 15. Effect of banding in the kinetics of carbon during partitioning. The effects of banding are shown in the top row for the carbon de-trapping from martensite defects and in the bottom row for the austenite enrichment. The maps show the simulated carbon concentration that is trapped in martensite in (a) a homogeneous microstructure and (b) a banded microstructure after 100 s of annealing at 400 °C. Both microstructures have $f^\gamma = 0.10$. (For interpretation of the references to color in this figure legend, the reader is referred to the web version of this article.)

Fig. 16. Effects of annealing on the distribution of carbon clustering to defects shown for different microstructures. The graph shows the cumulative distribution of carbon concentration trapped at martensite defects for all modeled microstructures we used in the present investigations, quantified for the quenched state and for the simulated annealed (at 400 °C for 100 s).

Table 1
Rate of austenite enrichment, indicated by the half-time $t_{1/2}$, for different microstructures, including, and excluding, the effect of segregation to defects.

f^γ \ k_C^{defects}	0 (no defects)	$7 \cdot 10^{-15}\text{m}^2$
$f^\gamma = 0.02$	3	28
$f^\gamma = 0.05$	3	31
$f^\gamma = 0.1$	3	35
$f^\gamma = 0.1$ - banded	6	66
$f^\gamma = 0.22$	1	25
$f^\gamma = 0.28$	1	22

equilibrium concentration. Here, any difference is directly related to the size of the retained austenite grains, which, as discussed earlier, is such that small austenite grains tend to be more enriched.

In contrast, in the banded microstructure, the austenite enrichment is more associated with the local surroundings (local phase fractions) rather than the size of austenite. For example, the pink colored pixels in the bottom image of Fig. 15b are located primarily on the sides of the RVE.

3.4. Final remarks

Fig. 16 shows the cumulative distributions of the trapped-carbon concentration for each microstructure at the quenched and annealed (100 s) state. Initially, all microstructures have a very narrow distribution, which is essentially brought about by any heterogeneity of the misorientation distribution shown earlier in Fig. 6. However, during annealing the carbon trapping at defects leads to a much stronger heterogeneity in the carbon distribution. In addition, although partitioning to austenite causes carbon de-trapping in all austenite–martensite RVEs (Fig. 13), there are still martensite volume elements containing high concentrations of trapped carbon. This explains why in QP steels, for example, a high carbon enrichment in austenite [22,51] is typically observed, while at the same time pronounced segregation within martensite is found [52]. In fact, Thomas et al. [51] also found an overall reduction of carbon segregation to dislocation/boundaries, especially after large annealing times.

The effect of carbon segregation to defects on austenite enrichment is shown in Table 1. The values shown correspond to the half-time $t_{1/2}$, i.e. the time at which half of the carbon-concentration change required to reach equilibrium has taken place. In all cases the effect of carbon trapping at defects on the pace at which austenite enriches is significant — almost in all cases the process is slowed down by a factor 10.

Overall, increasing the austenite fraction does not necessarily lead to reaching the equilibrium faster, as discussed earlier in Section 3.3.1. It is, however, clear that between the different microstructural aspects, banding is undesired when it comes to the pace of carbon de-trapping from martensite defects.

Regarding the evolution of carbon trapping at defects as a function of the austenite fraction, the simulated results indicate that partitioning suffers more from carbon trapping at defects for small austenite fractions. This explains why during annealing of almost fully martensitic
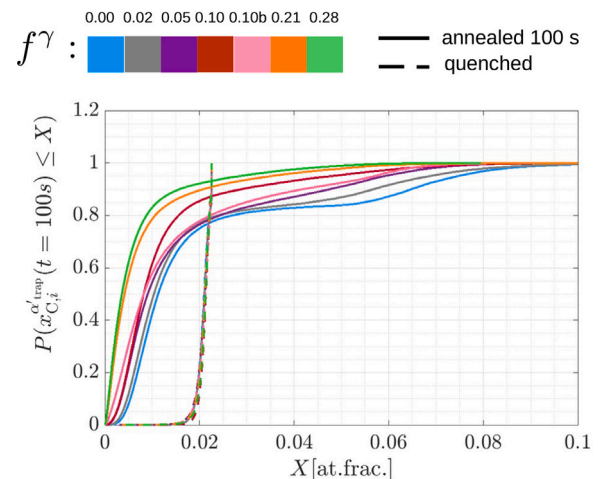
materials carbon segregation to defects is more pronounced, e. g. in [7, 8], whereas in QP steels (e. g. with austenite fractions more than 20%) almost all carbon is found in austenite.

Carbon trapping at defects in martensite does not only affect the kinetics of austenite enrichment, but also the local concentrations of carbon. This is an important point since it affects the properties and behavior of the produced microstructure [53]. The defects in the martensitic phase in an austenite/martensite microstructure, by trapping a fraction of the carbon, influence the eventual carbon concentration in the austenite and thus the stability of the austenite. This includes both the thermal stability during cooling to room temperature or a lower temperature and the mechanical stability against the so-called TRIP effect. Additionally, the local and global ductility of martensitic structures containing retained austenite is affected by the presence (and hence stabilization) of austenite [9,54–57].

Regarding the model's assumptions on the carbon enrichment ratio per defect (Eq. (2)), here a universal proportionality is taken between free- and trapped-carbon concentrations, i.e. a constant value for k_C^{defects} [m²] regardless of the magnitude of the concentrations and the defect types and density. This is a rough approximation, since the segregation takes place differently: (a) for different carbon concentrations (e.g. the proportionality of Cottrell would not extend for higher carbon concentrations), (b) between different defect types (e.g. isolated versus geometrically-necessary dislocations) and (c) between different defect densities, e.g. isolated versus interacting defects. Also, the overall defect density that was chosen in this work should be considered as a minimum value, since the boundary density was not considered. A physically reliable method to combine the densities of the two defect types will be developed in future work. Therefore, it is expected

that modifications of Eq. (2) in future applications will lead to more accurate predictions.

Finally, although here we applied the model in austenite–martensite microstructures assuming a stationary interface, a similar approach for carbon partitioning to austenite can be incorporated in modeling many other associated phenomena which depend on the local or global austenite enrichment. For example this approach can be combined in describing the local dependence of interface migration in martensite–austenite, e. g. in [11], and bainite formation, e. g. in [58]. Similarly, the mean field description of carbon equilibrium in the presence of defects proposed here can be incorporated in the global descriptions of equilibrium phase fractions [59] or bainite formation [60].

4. Conclusions

We presented a physics-based model for carbon redistribution in solid solution, realized by concentration gradient-driven diffusion, under the consideration of carbon trapping at defects and interphase partitioning. The main remarks of the proposed approach are:

- It enables the description of martensite as a phase different from ferrite, when it comes to carbon in relation with defects. This is important because, in view of the high defect density of martensite compared to ferrite, its overall carbon solubility is higher.
- It explains the de-trapping process, i.e. why in martensite-austenite microstructures before partitioning carbon is almost entirely found at martensite defects, whereas during annealing carbon enrichment in austenite is indeed taking place.
- The model is capable of reproducing the interaction between carbon trapping/de-trapping at martensite defects and interphase partitioning, also locally and through time. Also, the simulations are significantly stable against grid-settings, which is important in view of the different scale that the concurrent processes take place.

We applied the model in several martensite–austenite microstructures, analytically as well as obtained by EBSD, starting from full martensite. The main findings are summarized below:

- During annealing carbon segregation to martensite defects becomes much more heterogeneous, in comparison to the quenched state, such that (sub)block boundaries become or remain enriched and bulk martensite becomes depleted.
- Increasing the austenite fraction results in less carbon segregation to defects in martensite during annealing. This is realized by the global equilibrium as well as by the kinetics of carbon de-trapping from martensite defects.
- The kinetics of austenite enrichment during partitioning are much slower when carbon segregation to martensite defects is considered, compared to the case where it is neglected.
- Microstructure banding delays significantly the austenite enrichment during partitioning, especially when carbon segregation to defects in martensite is considered.

CRediT authorship contribution statement

Konstantina Traka: Writing – original draft, Validation, Software, Methodology, Investigation, Data curation, Conceptualization. **Jilt Sietsma:** Writing – review & editing, Supervision, Resources. **Maria J. Santofimia Navarro:** Writing – review & editing, Supervision, Resources, Project administration, Funding acquisition.

Declaration of competing interest

The authors declare that they have no known competing financial interests or personal relationships that could have appeared to influence the work reported in this paper.

Code availability

The code used in the present study cannot be shared at the moment due to legal reasons. However, the source files will be soon made available open source in OMicroN (optimizing microstructures numerically).

Acknowledgments

Appendix A. Supplementary data

Supplementary material related to this article can be found online at https://doi.org/10.1016/j.actamat.2024.120204.

References

[1] Tadao Watanabe, Sadahiro Tsurekawa, The control of brittleness and development of desirable mechanical properties in polycrystalline systems by grain boundary engineering, Acta Mater. (ISSN: 13596454) 47 (15–16) (1999) 4171–4185, http://dx.doi.org/10.1016/S1359-6454(99)00275-X, URL https://linkinghub.elsevier.com/retrieve/pii/S135964549900275X.

[2] D. Mattissen, D. Raabe, F. Heringhaus, Experimental investigation and modeling of the influence of microstructure on the resistive conductivity of a Cu–Ag–Nb in situ composite, Acta Mater. (ISSN: 13596454) 47 (5) (1999) 1627–1634, http://dx.doi.org/10.1016/S1359-6454(99)00026-9, URL https://linkinghub.elsevier.com/retrieve/pii/S1359645499000269.

[3] Zhaoliang Li, Junhang Chen, Wei Xue, Chenghui Yin, Jialiang Song, Kui Xiao, Role of segregation behavior of Cu and Sb in the region of inclusions on initial corrosion, npj Mater. Degrad. (ISSN: 2397-2106) 7 (1) (2023) 29, http://dx.doi.org/10.1038/s41529-023-00354-5, URL https://www.nature.com/articles/s41529-023-00354-5.

[4] Günter Gottstein, Physical Foundations of Materials Science, Springer Berlin Heidelberg, Berlin, Heidelberg, ISBN: 978-3-662-09291-0, 2004, http://dx.doi.org/10.1007/978-3-662-09291-0 URL http://link.springer.com/10.1007/978-3-662-09291-0.

[5] Z.Y. Chang, Y.J. Li, D. Wu, Enhanced ductility and toughness in 2000 MPa grade press hardening steels by auto-tempering, Mater. Sci. Eng. A (ISSN: 09215093) 784 (2020) 139342, http://dx.doi.org/10.1016/j.msea.2020.139342, URL https://linkinghub.elsevier.com/retrieve/pii/S0921509320304238.

[6] B. Kim, J. Sietsma, M.J. Santofimia, Thermodynamic aspects of carbon redistribution during ageing and tempering of Fe–Ni–C alloys, Phil. Mag. 96 (25) (2016) 2632–2648, http://dx.doi.org/10.1080/14786435.2016.1211790 (ISSN 1478-6435, 1478-6443) URL https://www.tandfonline.com/doi/full/10.1080/14786435.2016.1211790.

[7] L. Yuan, D. Ponge, J. Wittig, P. Choi, J.A. Jiménez, D. Raabe, Nanoscale austenite reversion through partitioning, segregation and kinetic freezing: Example of a ductile 2GPa Fe–Cr–C steel, Acta Mater. (ISSN: 13596454) 60 (6–7) (2012) 2790–2804, http://dx.doi.org/10.1016/j.actamat.2012.01.045, URL https://linkinghub.elsevier.com/retrieve/pii/S1359645412000833.

[8] D. Raabe, S. Sandlöbes, J. Millán, D. Ponge, H. Assadi, M. Herbig, P.-P. Choi, Segregation engineering enables nanoscale martensite to austenite phase transformation at grain boundaries: A pathway to ductile martensite, Acta Mater. (ISSN: 13596454) 61 (16) (2013) 6132–6152, http://dx.doi.org/10.1016/j.actamat.2013.06.055, URL https://linkinghub.elsevier.com/retrieve/pii/S1359645413005004.

[9] J. Hidalgo, K.O. Findley, M.J. Santofimia, Thermal and mechanical stability of retained austenite surrounded by martensite with different degrees of tempering, Mater. Sci. Eng. A (ISSN: 09215093) 690 (2017) 337–347, http://dx.doi.org/10.1016/j.msea.2017.03.017, URL https://linkinghub.elsevier.com/retrieve/pii/S0921509317303064.

[10] J. Speer, D.K. Matlock, B.C. De Cooman, J.G. Schroth, Carbon partitioning into austenite after martensite transformation, Acta Mater. (ISSN: 1359-6454) 51 (9) (2003) 2611–2622, http://dx.doi.org/10.1016/S1359-6454(03)00059-4, URL https://linkinghub.elsevier.com/retrieve/pii/S1359645403000594.

[11] M.J. Santofimia, L. Zhao, J. Sietsma, Model for the interaction between interface migration and carbon diffusion during annealing of martensite–austenite microstructures in steels, Scr. Mater. (ISSN: 13596462) 59 (2) (2008) 159–162, http://dx.doi.org/10.1016/j.scriptamat.2008.02.045, URL https://linkinghub.elsevier.com/retrieve/pii/S1359646208001930.

[12] Yuki Toji, Goro Miyamoto, Dierk Raabe, Carbon partitioning during quenching and partitioning heat treatment accompanied by carbide precipitation, Acta Mater. (ISSN: 13596454) 86 (2015) 137–147, http://dx.doi.org/10.1016/j.actamat.2014.11.049, URL https://linkinghub.elsevier.com/retrieve/pii/S1359645414009021.

[13] Zongbiao Dai, Zhigang Yang, Chi Zhang, Hao Chen, Incomplete carbon partitioning during quenching and partitioning of Fe–C–Mn–Si steels: Modeling and experimental validations, Acta Mater. (ISSN: 13596454) 200 (2020) 597–607, http://dx.doi.org/10.1016/j.actamat.2020.09.045, URL https://linkinghub.elsevier.com/retrieve/pii/S1359645420307394.

[14] Aarne Pohjonen, Shashank Ramesh Babu, Ville-Valtteri Visuri, Coupled model for carbon partitioning, diffusion, Cottrell atmosphere formation and cementite precipitation in martensite during quenching, Comput. Mater. Sci. (ISSN: 09270256) 209 (2022) 111413, http://dx.doi.org/10.1016/j.commatsci.2022.111413, URL https://linkinghub.elsevier.com/retrieve/pii/S0927025622001823.

[15] Osamu Waseda, Roberto G.A. Veiga, Julien Morthomas, Patrice Chantrenne, Charlotte S. Becquart, Fabienne Ribeiro, Andrei Jelea, Helio Goldenstein, Michel Perez, Formation of carbon Cottrell atmospheres and their effect on the stress field around an edge dislocation, Scr. Mater. (ISSN: 13596462) 129 (2017) 16–19, http://dx.doi.org/10.1016/j.scriptamat.2016.09.032, URL https://linkinghub.elsevier.com/retrieve/pii/S1359646216304602.

[16] A.H. Cottrell, D.L. Dexter, Dislocations and plastic flow in crystals, Am. J. Phys. (ISSN: 1943-2909) 22 (4) (1954) 242–243, http://dx.doi.org/10.1119/1.1933704 URL http://aapt.scitation.org/doi/10.1119/1.1933704.

[17] A.H. Cottrell, M.A. Jaswon, Distribution of solute atoms round a slow dislocation, Proc. Royal Soc. Lond. Ser. A 199 (1056) (1949) 104–114, http://dx.doi.org/10.1098/rspa.1949.0128.

[18] A.H. Cottrell, B.A. Bilby, Dislocation theory of yielding and strain ageing of iron, Proc. Phys. Soc. Sec. A (ISSN: 0370-1298) 62 (1) (1949) 49–62, http://dx.doi.org/10.1088/0370-1298/62/1/308, URL https://iopscience.iop.org/article/10.1088/0370-1298/62/1/308.

[19] I. Medouni, A. Portavoce, P. Maugis, P. Eyméoud, M. Yescas, K. Hoummada, Role of dislocation elastic field on impurity segregation in Fe-based alloys, Sci. Rep. (ISSN: 2045-2322) 11 (1) (2021) 1780, http://dx.doi.org/10.1038/s41598-020-80140-4, URL http://www.nature.com/articles/s41598-020-80140-4.

[20] M. Herbig, D. Raabe, Y.J. Li, P. Choi, S. Zaefferer, S. Goto, Atomic-scale quantification of grain boundary segregation in nanocrystalline material, Phys. Rev. Lett. (ISSN: 1079-7114) 112 (12) (2014) 126103, http://dx.doi.org/10.1103/PhysRevLett.112.126103 URL https://link.aps.org/doi/10.1103/PhysRevLett.112.126103.

[21] Bevis Hutchinson, Joacim Hagström, Oskar Karlsson, David Lindell, Malin Tornberg, Fredrik Lindberg, Mattias Thuvander, Microstructures and hardness of as-quenched martensites (0.1–0.5% C), Acta Mater. (ISSN: 13596454) 59 (14) (2011) 5845–5858, http://dx.doi.org/10.1016/j.actamat.2011.05.061, URL https://linkinghub.elsevier.com/retrieve/pii/S1359645411004010.

[22] Yuki Toji, Hiroshi Matsuda, Michael Herbig, Pyuck-Pa Choi, Dierk Raabe, Atomic-scale analysis of carbon partitioning between martensite and austenite by atom probe tomography and correlative transmission electron microscopy, Acta Mater. (ISSN: 13596454) 65 (2014) 215–228, http://dx.doi.org/10.1016/j.actamat.2013.10.064, URL https://linkinghub.elsevier.com/retrieve/pii/S1359645413008276.

[23] J.S. Koehler, On the dislocation theory of plastic deformation, Phys. Rev. (ISSN: 0031-899X) 60 (5) (1941) 397–410, http://dx.doi.org/10.1103/PhysRev.60.397, URL https://link.aps.org/doi/10.1103/PhysRev.60.397.

[24] Irving Langmuir, The adsorption of gases on plane surfaces of glass, mica and platinum, J. Am. Chem. Soc. (ISSN: 1520-5126) 40 (9) (1918) 1361–1403, http://dx.doi.org/10.1021/ja02242a004 URL https://pubs.acs.org/doi/abs/10.1021/ja02242a004.

[25] D. McLean, A. Maradudin, Grain boundaries in metals, Phys. Today (ISSN: 1945-0699) 11 (7) (1958) 35–36, http://dx.doi.org/10.1063/1.3062658 URL http://physicstoday.scitation.org/doi/10.1063/1.3062658.

[26] S. Matas, R.F. Hehemann, Retained austenite and the tempering of martensite, Nature (ISSN: 1476-4687) 187 (4738) (1960) 685–686, http://dx.doi.org/10.1038/187685a0 URL https://www.nature.com/articles/187685a0.

[27] M.G. Mecozzi, J. Eiken, M.J. Santofimia, J. Sietsma, Phase field modelling of microstructural evolution during the quenching and partitioning treatment in low-alloy steels, Comput. Mater. Sci. (ISSN: 09270256) 112 (2016) 245–256, http://dx.doi.org/10.1016/j.commatsci.2015.10.048, URL https://linkinghub.elsevier.com/retrieve/pii/S0927025615007053.

[28] Y. Takahama, M.J. Santofimia, M.G. Mecozzi, L. Zhao, J. Sietsma, Phase field simulation of the carbon redistribution during the quenching and partitioning process in a low-carbon steel, Acta Mater. (ISSN: 13596454) 60 (6–7) (2012) 2916–2926, http://dx.doi.org/10.1016/j.actamat.2012.01.055, URL https://linkinghub.elsevier.com/retrieve/pii/S1359645412000936.

[29] Adolf Fick, Ueber diffusion, Ann. Phys. Chem. (ISSN: 1521-3889) 170 (1) (1855) 59–86, http://dx.doi.org/10.1002/andp.18551700105 URL https://onlinelibrary.wiley.com/doi/10.1002/andp.18551700105.

[30] J. Wilde, A. Cerezo, G.D.W Smith, Three-dimensional atomic-scale mapping of a cottrell atmosphere around a dislocation in iron, Scr. Mater. (ISSN: 13596462) 43 (1) (2000) 39–48, http://dx.doi.org/10.1016/S1359-6462(00)00361-4, URL https://linkinghub.elsevier.com/retrieve/pii/S1359646200003614.

[31] S. Morito, J. Nishikawa, T. Maki, Dislocation density within lath martensite in Fe-C and Fe-Ni alloys, ISIJ Int. (ISSN: 0915-1559) 43 (9) (2003) 1475–1477, http://dx.doi.org/10.2355/isijinternational.43.1475, URL http://www.jstage.jst.go.jp/article/isijinternational1989/43/9/43_9_1475/_article.

[32] E.I. Galindo-Nava, P.E.J. Rivera-Díaz-del-Castillo, A model for the microstructure behaviour and strength evolution in lath martensite, Acta Mater. (ISSN: 13596454) 98 (2015) 81–93, http://dx.doi.org/10.1016/j.actamat.2015.07.018, URL https://linkinghub.elsevier.com/retrieve/pii/S1359645415004802.

[33] Predrag Andric, Sebastián Echeverri Restrepo, Francesco Maresca, Predicting dislocation density in martensite ab-initio, Acta Mater. (ISSN: 13596454) 243 (2023) 118500, http://dx.doi.org/10.1016/j.actamat.2022.118500, URL https://linkinghub.elsevier.com/retrieve/pii/S1359645422008771.

[34] J. Svoboda, G.A. Zickler, E. Kozeschnik, F.D. Fischer, Kinetics of interstitial segregation in Cottrell atmospheres and grain boundaries, Phil. Mag. Lett. (ISSN: 1362-3036) 95 (9) (2015) 458–465, http://dx.doi.org/10.1080/09500839.2015.1087652 URL http://www.tandfonline.com/doi/full/10.1080/09500839.2015.1087652.

[35] Juan Macchi, Julien Teixeira, Frédéric Danoix, Guillaume Geandier, Sabine Denis, Frédéric Bonnet, Sébastien Y.P. Allain, Impact of carbon segregation on transition carbides and cementite precipitation during tempering of low carbon steels: Experiments and modeling, Acta Mater. (ISSN: 13596454) 272 (2024) 119919, http://dx.doi.org/10.1016/j.actamat.2024.119919, URL https://linkinghub.elsevier.com/retrieve/pii/S1359645424002726.

[36] M. Hillert, J. Ågren, On the definitions of paraequilibrium and orthoequilibrium, Scr. Mater. (ISSN: 13596462) 50 (5) (2004) 697–699, http://dx.doi.org/10.1016/j.scriptamat.2003.11.020, URL https://linkinghub.elsevier.com/retrieve/pii/S1359646203007425.

[37] M. Hillert, J. Ågren, Reply to comments on "On the definition of paraequilibrium and orthoequilibrium", Scr. Mater. (ISSN: 13596462) 52 (1) (2005) 87–88, http://dx.doi.org/10.1016/j.scriptamat.2004.08.026, URL https://linkinghub.elsevier.com/retrieve/pii/S1359646204004932.

[38] Sachin Kumar, Shiv Brat Singh, Evolution of microstructure during the "quenching and partitioning (Q&P)" treatment, Materialia (ISSN: 25891529) 18 (2021) 101135, http://dx.doi.org/10.1016/j.mtla.2021.101135, URL https://linkinghub.elsevier.com/retrieve/pii/S2589152921001381.

[39] D.T. Pierce, D.R. Coughlin, K.D. Clarke, E. De Moor, J. Poplawsky, D.L. Williamson, B. Mazumder, J.G. Speer, A. Hood, A.J. Clarke, Microstructural evolution during quenching and partitioning of 0.2C-1.5Mn-1.3Si steels with Cr or Ni additions, Acta Mater. (ISSN: 13596454) 151 (2018) 454–469, http://dx.doi.org/10.1016/j.actamat.2018.03.007, URL https://linkinghub.elsevier.com/retrieve/pii/S1359645418301861.

[40] Sachin Kumar, Quenching and partitioning (Q&P) process: A critical review of the competing reactions, Mater. Sci. Technol. (ISSN: 1743-2847) 38 (11) (2022) 663–675, http://dx.doi.org/10.1080/02670836.2022.2062646 URL http://journals.sagepub.com/doi/10.1080/02670836.2022.2062646.

[41] M.J. Santofimia, L. Zhao, J. Sietsma, Overview of mechanisms involved during the quenching and partitioning process in steels, Metall. Mater. Trans. A (ISSN: 1543-1940) 42 (12) (2011) 3620–3626, http://dx.doi.org/10.1007/s11661-011-0706-z URL http://link.springer.com/10.1007/s11661-011-0706-z.

[42] John Ågren, Diffusion in phases with several components and sublattices, J. Phys. Chem. Solids (ISSN: 00223697) 43 (5) (1982) 421–430, http://dx.doi.org/10.1016/0022-3697(82)90152-4, URL https://linkinghub.elsevier.com/retrieve/pii/0022369782901524.

[43] John Ågren, A revised expression for the diffusivity of carbon in binary Fe-C austenite, Scr. Metall. (ISSN: 00369748) 20 (11) (1986) 1507–1510, http://dx.doi.org/10.1016/0036-9748(86)90384-4, URL https://linkinghub.elsevier.com/retrieve/pii/0036974886903844.

[44] C. Bos, M.G. Mecozzi, J. Sietsma, A microstructure model for recrystallisation and phase transformation during the dual-phase steel annealing cycle, Comput. Mater. Sci. (ISSN: 09270256) 48 (3) (2010) 692–699, http://dx.doi.org/10.1016/j.commatsci.2010.03.010, URL https://linkinghub.elsevier.com/retrieve/pii/S0927025610001242.

[45] C. Bos, M.G. Mecozzi, D.N. Hanlon, M.P. Aarnts, J. Sietsma, Application of a three-dimensional microstructure evolution model to identify key process settings for the production of dual-phase steels, Metall. Mater. Trans. A (ISSN: 1543-1940) 42 (12) (2011) 3602–3610, http://dx.doi.org/10.1007/s11661-011-0696-x URL https://link.springer.com/10.1007/s11661-011-0696-x.

[46] Konstantina Traka, Karo Sedighiani, Cornelis Bos, Jesus Galan Lopez, Katja Angenendt, Dierk Raabe, Jilt Sietsma, Topological aspects responsible for recrystallization evolution in an IF-steel sheet – Investigation with cellular-automaton simulations, Comput. Mater. Sci. (ISSN: 09270256) 198 (2021) 110643, URL https://linkinghub.elsevier.com/retrieve/pii/S0927025621003700.

[47] V. Shah, K. Sedighiani, J.S. Van Dokkum, C. Bos, F. Roters, M. Diehl, Coupling crystal plasticity and cellular automaton models to study meta-dynamic recrystallization during hot rolling at high strain rates, Mater. Sci. Eng. A (ISSN: 09215093) 849 (2022) 143471, http://dx.doi.org/10.1016/j.msea.2022.143471, URL https://linkinghub.elsevier.com/retrieve/pii/S0921509322008590.

[48] M.F. Ashby, The deformation of plastically non-homogeneous materials, Philos. Mag. A J. Theor. Exp. Appl. Phys. (ISSN: 0031-8086) 21 (170) (1970) 399–424, http://dx.doi.org/10.1080/14786437008238426, URL https://www.tandfonline.com/doi/full/10.1080/14786437008238426.

[49] L. Morsdorf, C.C. Tasan, D. Ponge, D. Raabe, 3D structural and atomic-scale analysis of lath martensite: Effect of the transformation sequence, Acta Mater. (ISSN: 1359-6454) 95 (2015) 366–377, http://dx.doi.org/10.1016/j.actamat.2015.05.023, URL https://linkinghub.elsevier.com/retrieve/pii/S1359645415003444.

[50] David Turnbull, Theory of grain boundary migration rates, JOM (ISSN: 1543-1851) 3 (8) (1951) 661–665, http://dx.doi.org/10.1007/BF03397362 URL http://link.springer.com/10.1007/BF03397362.

[51] Grant Aaron Thomas, Frederic Danoix, John Gordon Speer, Steven William Thompson, Fabien Cuvilly, Carbon atom Re-distribution during quenching and partitioning, ISIJ Int. (ISSN: 1347-5460) 54 (12) (2014) 2900–2906, http://dx.doi.org/10.2355/isijinternational.54.2900 URL https://www.jstage.jst.go.jp/article/isijinternational/54/12/54_2900/_article.

[52] M. Kuzmina, D. Raabe, W. Bleck, Segregation Driven Phase Transformation in Medium Mn Steel (Ph.D. thesis), RWTH Aachen University, Germany, 2015, URL urn:nbn:de:hbz:82-rwth-2015-050112.

[53] Dierk Raabe, Binhan Sun, Alisson Kwiatkowski Da Silva, Baptiste Gault, Hung-Wei Yen, Karo Sedighiani, Prithiv Thoudden Sukumar, Isnaldi R. Souza Filho, Shyam Katnagallu, Eric Jägle, Philipp Kürnsteiner, Navyanth Kusampudi, Leigh Stephenson, Michael Herbig, Christian H. Liebscher, Hauke Springer, Stefan Zaefferer, Vitesh Shah, Su-Leen Wong, Christian Baron, Martin Diehl, Franz Roters, Dirk Ponge, Current challenges and opportunities in microstructure-related properties of advanced high-strength steels, Metall. Mater. Trans. A (ISSN: 1543-1940) 51 (11) (2020) 5517–5586, http://dx.doi.org/10.1007/s11661-020-05947-2 URL https://link.springer.com/10.1007/s11661-020-05947-2.

[54] M.J. Santofimia, T. Nguyen-Minh, L. Zhao, R. Petrov, I. Sabirov, J. Sietsma, New low carbon Q&P steels containing film-like intercritical ferrite, Mater. Sci. Eng. A (ISSN: 09215093) 527 (23) (2010) 6429–6439, http://dx.doi.org/10.1016/j.msea.2010.06.083, URL https://linkinghub.elsevier.com/retrieve/pii/S0921509310007161.

[55] K.O. Findley, J. Hidalgo, R.M. Huizenga, M.J. Santofimia, Controlling the work hardening of martensite to increase the strength/ductility balance in quenched and partitioned steels, Mater. Des. (ISSN: 02641275) 117 (2017) 248–256, http://dx.doi.org/10.1016/j.matdes.2016.12.065, URL https://linkinghub.elsevier.com/retrieve/pii/S026412751631591X.

[56] F. Maresca, W.A. Curtin, The austenite/lath martensite interface in steels: Structure, athermal motion, and in-situ transformation strain revealed by simulation and theory, Acta Mater. (ISSN: 13596454) 134 (2017) 302–323, http://dx.doi.org/10.1016/j.actamat.2017.05.044, URL https://linkinghub.elsevier.com/retrieve/pii/S1359645417304317.

[57] F. Maresca, V.G. Kouznetsova, M.G.D. Geers, On the role of interlath retained austenite in the deformation of lath martensite, Modelling Simul. Mater. Sci. Eng. (ISSN: 1361-651X) 22 (4) (2014) 045011, http://dx.doi.org/10.1088/0965-0393/22/4/045011 URL https://iopscience.iop.org/article/10.1088/0965-0393/22/4/045011.

[58] Arthur S. Nishikawa, Maria J. Santofimia, Jilt Sietsma, Hélio Goldenstein, Influence of bainite reaction on the kinetics of carbon redistribution during the Quenching and Partitioning process, Acta Mater. (ISSN: 13596454) 142 (2018) 142–151, http://dx.doi.org/10.1016/j.actamat.2017.09.048, URL https://linkinghub.elsevier.com/retrieve/pii/S1359645417308145.

[59] Amit K. Behera, G.B. Olson, Nonequilibrium thermodynamic modeling of carbon partitioning in quench and partition (Q&P) steel, Scr. Mater. (ISSN: 13596462) 147 (2018) 6–10, http://dx.doi.org/10.1016/j.scriptamat.2017.12.027, URL https://linkinghub.elsevier.com/retrieve/pii/S1359646217307273.

[60] Daniel Dos Santos Avila, S. Erik Offerman, Maria J. Santofimia, Modeling the effect of prior austenite grain size on bainite formation kinetics, Acta Mater. (ISSN: 13596454) 266 (2024) 119656, http://dx.doi.org/10.1016/j.actamat.2024.119656, URL https://linkinghub.elsevier.com/retrieve/pii/S1359645424000090.